Local Time Asymmetries and Toroidal Field Line Resonances: Global Magnetospheric Modeling in SWMF

S.M. Ellington[1], M.B. Moldwin[2], M.W. Liemohn[2]

[1]Applied Physics, University of Michigan, Ann Arbor, Michigan, USA

[2]Climate and Space Sciences and Engineering, University of Michigan, Ann Arbor, Michigan, USA

Abstract. We present evidence of resonant wave-wave coupling via toroidal field line resonance (FLR) signatures in the Space Weather Modeling Framework's (SWMF) global, terrestrial magnetospheric model in one simulation driven by a synthetic upstream solar wind with embedded broadband dynamic pressure fluctuations. Using *in situ*, stationary point measurements of the radial electric field along the 1500 LT meridian, we show that SWMF reproduces a multi-harmonic, continuous distribution of FLRs exemplified by 180° phase reversals and amplitude peaks across the resonant L shells. By linearly increasing the amplitude of the dynamic pressure fluctuations in time, we observe a commensurate increase in the amplitude of the radial electric and azimuthal magnetic field fluctuations, which is consistent with the solar wind driver being the dominant source of the fast mode energy. While we find no discernible local time changes in the FLR frequencies despite large-scale, monotonic variations in the dayside equatorial mass density, in selectively sampling resonant points and examining spectral resonance widths, we observe significant radial, harmonic, and time dependent local time asymmetries in the radial electric field amplitudes. A weak but persistent local time asymmetry exists in measures of the estimated coupling efficiency between the fast mode and toroidal wave fields, which exhibits a radial dependence consistent with the coupling strength examined by Mann et al. [1999] and Zhu and Kivelson [1988]. We discuss internal structural mechanisms and additional external energy sources that may account for these asymmetries as we find that local time variations in the strength of the compressional driver

are not the predominant source of the FLR amplitude asymmetries. These include resonant mode coupling of observed Kelvin-Helmholtz (KH) surface wave generated Pc5 band ultra-low frequency (ULF) pulsations, local time differences in local ionospheric dampening rates, and variations in azimuthal mode number, which may impact the partitioning of spectral energy between the toroidal and poloidal wave modes.

1. Introduction

In the collisionless, inhomogeneous plasmas typical of the terrestrial magnetosphere, global ULF waves are an important energy transport mechanism. With fundamental wavelengths on the order of the magnetospheric cavity, ULF waves in the Pc3-5 category with frequencies between 2 and 100 mHz are known to mediate the long-range relaxation of internally driven kinetic instabilities [*Cheng et al.*, 1994] and externally driven compressional disturbances generated in the interaction of the solar wind with the magnetosphere. There are numerous sources of these waves. Examples include drift-mirror type instabilities borne from plasma temperature anisotropy–a potential source for the energization of the radiation belt electrons [*Hasegawa*, 1969;*Elkington et al.*, 1999]; the Kelvin-Helmholtz instability, which arises due to the buffeting of the magnetopause to high-speed solar wind events; resonantly excited surface waves along the magnetopause [*Mann et al.*, 1999]; and dynamic pressure fluctuations in the upstream solar wind [*Takahashi et al.*, 1988], which is the focus of this paper.

A field line resonance is a particular coupling phenomenon between global, fast magnetosonic and localized shear Alfvén waves and have long been used to explain the latitudinally-dependent wave amplitude and frequency spectra observed by satellites and ground-based magnetometers [*Engebretson*, 1987]. Broadband excitations at the magnetopause are a well-known source of these waves, and many have explored a variety of paradigms to reconcile observations of field line resonances with the ongoing development of the theory [*Kivelson et al.*, 1986; *Samson et al.*, 1992]. Kivelson et al. [1986] modeled the closed dipole field with a box geometry with perfectly conducting magnetopause and ionospheric boundaries using ideal magnetohydrodynamics (MHD), where FLRs appeared as singularities in the coupled wave equations. Observational evidence of FLRs at discrete frequencies in the nightside have led Samson et al. [1992] to invoke a waveguide model to explore the propagation of wave modes between the magnetopause and turning points at the inner boundary of the magnetospheric cavity.

The field-line curvature, density distribution and gradients significantly impact the spectra, nodal and harmonic structure of these wave modes [*Radoski et al.*, 1966; *Mann et al.*, 1995]. The finite conductivity of the magnetospheric boundaries, wave-particle interactions on kinetic scales, and the generation of parallel electric fields can all dampen shear Alfvén waves through field aligned currents that close in the ionosphere, dissipate through Joule heating, and wave mode decay and phase mixing [*Newton et al.*, 1978; *Mann et al.*, 1995; *Sarris et al.*, 2009]. The amplitude peak at the resonant L shell balances the compressional energy with these loss mechanisms, and the resonance condition entails a radial 180 phase reversal across the singular point [*Kivelson et al.*, 1986].

Numerous studies have observed and examined a significant local time asymmetry in the occurrence rate and amplitude of field line resonances driven by Pc5 pulsations [*Nosé et al.*, 1995; *Chisham et al.*, 1997; *Mann et al.*, 1999; *Glassmeier et al.*, 2000]. Mann et al. [1999] for instance find evidence that the more pronounced occurrence and amplitude in the dawn quadrant is due to the coupling of magnetopause shear-flow instabilities to the magnetospheric cavity and over-reflection of waveguide modes generated by solar wind dynamic pressure. Satellite observations bear out this hypothesis. Concerning measures of the coupling efficiency between the compressional driver and standing wave modes, Mann et al. [1999] and Zhu and Kivelson [1988] show using numerical models an azimuthal mode number and radial dependence by integrating the total, time-dependent Alfvénic energy across the domain assuming a single frequency driver. Measuring the coupling rate is important because it gives the amount of energy made available by the resonant coupling, the mechanism therein, and how numerical or local plasma conditions may impact the mode coupling process. We note that no global magnetospheric model has been used to explore local time asymmetries in FLR amplitudes nor the coupling rate, despite the need to quantify and examine the mechanisms impacting the partioning of energy in wave mode conversion.

Analyzing resonant coupling mechanisms and quantifying wave coupling strengths in global magnetospheric models may be relevant to radiation belt studies. ULF waves are a well-known energization source of electrons through either radial diffusion from a noon-midnight asymmetric toroidal electric field or drift or bounce resonance with poloidal electric fields [*Hasegawa*, 1969;*Elkington et al.*, 1999]. The former would be a more likely explanation for the low azimuthal wave modes generated in this simulation, and FLRs would naturally be the only source of the toroidal wave fields.

Numerical modeling has been used to examine field line resonances, particularly the sources of the compressional energy, wave mode coupling mechanisms, and related phenomenona within various geometries. Degeling et al. [2010], for instance, used a linear MHD model of the magnetosphere to study the effect of compressed dipole fields on the spatiotemporal sources and generation mechanisms of fast mode and coupled shear Alfvén waves. The global magnetosphere, however, presents notable challenges to these models, even where non-linear processes are included. Claudepierre et al. [2010] were the first to show in the self-consistent, global MHD Lyon-Fedder-Mobarry model (LFM) that fluctuations in the upstream dynamic pressure can produce FLRs in the dayside magnetosphere and to show that they were driven by cavity modes. Even then, others argue that the discretization of Cartesian grids, such as in the SWMF model, and the Alfvén continuum dampen and obscure what is otherwise a localized resonance phenomena, which make them difficult to detect, particularly with broadband sources, or difficult to produce altogether [*Stellmacher et al.*, 1997]. Bellan [1996], for instance, showed that kinetic Alfvén waves mediate the coupling between fast and shear modes, which may suggest FLRs in MHD models are an unphysical, numerical artifact. This is particularly evident in cases where the grid resolution is much larger than the phase mixing length as the numerical solution may never converge. Additionally, the treatment of the ionosphere in global magnetospheric models is non-trivial as the ionosphere also plays a major role in the formation, structure, and dissipation of FLRs.

These outstanding issues compel us to test whether global magnetospheric models can reproduce field line resonances in a manner consistent with theory, though we note that very few if any have been validated systematically using observational data. The notable differences between global magnetospheric and ionospheric models allow us to explore a variety of mechanisms that impact the excitation and structure of field line resonances and to make improvements that may better reproduce FLRs and related wave-wave phenomena. The goal of this technical study is to show that the global magnetospheric model, SWMF, can produce FLRs–and generally speaking, the coupling of wave modes–using the solar wind as the compressional driver and to show that it can reproduce the local time asymmetries captured by numerous observation studies. Additionally, the linearly increasing amplitude of the dynamic pressure fluctuations used here often resembles the dynamic solar wind density profiles seen during periods of heightened geomagnetic activity, which allows us to observe the impact on FLRs and identify Alfvén-wave driven phenomena. The study broadly follows the design employed by Claudepierre et al. [2010], who used the LFM global MHD model.

2. Methodology and Simulation Results

2.1. Global Model

We use the SWMF global MHD model coupled with a self-consistent ionospheric electric potential solver with an inner boundary placed at 2.5 R_E [*Toth et al.*, 2005]. We set the inner boundary number density to 28 particles per cm^{-3} so that the fundamental and several harmonics of the field line eigenfrequencies would lie within the spectral bandwith of this simulation. The ionospheric conductance is set with an EUV solar flux of 100×10^{-22} J/m^2 and a 0.25 Siemen auroral oval Pedersen conductance. While the conductance within the auroral oval is much smaller than what other authors have used in numerical simulations, since the ionospheric conductance is regulated mostly by the EUV solar flux, the conductance values elsewhere are typical. SWMF uses a Cartesian grid and solves the single-fluid, ideal MHD equations using a non-conservative, second-order upwind scheme with a 0.125 R_E grid resolution throughout the dayside magnetospheric cavity. The solar wind and IMF serve as upstream boundary conditions at 32 R_E with open boundary conditions at 92 Re in the tail and +/- 92 R_E in the y and z-directions. A Boris correction to five percent the speed of light ensures a reasonable time step, and a partially implicit time-stepping scheme with a minimum time step of 5 seconds is used for stability. In this simulation, SWMF is not coupled to a plasmasphere or ring current model, which may underestimate the time-dependent ion density and pressure distribution in the inner magnetosphere. The magnetic axis is aligned with the rotational axis.

Shown in Figure 1, the upstream solar wind density profile includes broadband fluctuations between 0 and 100 mHz with a spectral resolution of 0.03 mHz. This spectral bandwidth matches the time cadence of the numerical solver. Table 1 shows a comparison with the Claudepierre et al. [2010] LFM simulation of several of the input parameters. There are two major differences between the two simulations aside from the ionospheric conductance: the inclusion of a linearly increasing in time fluctuations in the amplitude of the dynamic pressure to within a maximum envelope of 0 to 10 particles per cm^{-3} with a root mean average of 5; and a rotating dipole, which allows us to examine self-consistent diurnal impacts on ionospheric conductance and density distribution. We designed the driver as such as a trace to identify the solar wind driver as the driver of the FLRs, and indeed the amplitude of the FLRs grows continuously–albeit at different rates–with the amplitude of the pressure fluctuations and to see if we can drive ULF wave-mediated phenomena. We employ an average, quiet time solar wind velocity of 400 km/s and iniatilize SWMF in a steady-state mode for 5000 seconds in order to eliminate transient, global magnetospheric disturbances. We note that this may not have been sufficient to allow the magnetosphere to relax into a global equilibrium state. A northward B_z of 5 nT is maintained throughout the simulation run.

To examine the toroidal wave modes, we analyze the radial electric field component, E_r, in the equatorial plane at the 1500 LT meridian. We use stationary points located at 0.125 R_E increments from 3 to 11.875 R_E to sample the electric field at a 10 s cadence for 2 hours after the onset of the upstream pressure fluctuations, which together afford an approximately 0.1 mHz spectral resolution up to a Nyquist frequency of 50 mHz. We observe a similar attenuation of the high frequency–greater than 20 mHz–components of the broadband upstream density fluctuations as reported in Claudepierre et al. [2010]. We believe, however, that this is due to the 0.125 R_E grid resolution upstream of the bow shock. Given the Alfvén wave speeds of 50 km/s, the wavelengths of the frequency components greater than 20 mHz are about the width of 3 grid cells, which is much less than what is necessary to fully resolve those waves. Simulation runs with grid resolutions of about 1 R_E at the upstream boundary show a similar degree of attenuation above 10 mHz, which corroborates this interpretation.

We calculate the field line eigenfrequencies using the WKB approximation using Chi et al.'s [1998] calculations of the integral of the Alfvén wave speed along a dipolar field line given by

$$\tau = 1.9\times10^{-5} {n_0}^{1/2} L^4 \int_{\theta_S}^{\theta_N} \cos^{7-p}\theta \,\mathrm{d}\theta \tag{1}$$

which we solve numerically. The bounds of integration are between the north and south ionospheric footpoints of the field line for a given L shell, where n_0 is the plasma density at the equatorial crossing. The p value is the density power law scaling, which we calculate directly in our simulation from the radial profile of the ion density at the 1500 LT meridian. Since the Alfvén wave speed decreases linearly through the time period chosen for analysis, we take the average power law dependence of p=1.41. While Radoski et al. [1966] solved the toroidal wave equation exactly using a p=6 density law, the wave equation cannot be solved analytically for p=1.41, so we use the WKB approximation exclusively. Additionally, since noon meridional cuts show an axisymmetric density distribution, a power law fit of the radial density distribution in the equatorial plane is appropriate for the WKB approximation of the field-line eigenfrequencies.

The coupling between the global magnetospheric and ionospheric electric potential solver required careful consideration. Even though we allow the magnetic field lines to move at the inner boundary, we consider this boundary to be closed since the solver requires the electric and magnetic field perturbations to vanish in the region between the ionosphere and inner boundary. Since only the field aligned currents along the background, dipole field are mapped to and from the ionosphere, the inner boundary behaves as a node. Even if the gap region were included in the calculation of the eigenfrequencies, the contribution would decrease the eigenfrequencies by at most ten percent. However, this is well within the envelope of the observed spectral resonance widths of the radial electric field.

The time-dependent number density profile along the 1500 and 900 LT meridians is shown in Figure 2. We note that the increasing amplitude of the upstream pressure fluctuations is associated with a corresponding decrease in the Alfvén wave speed profile in the inner magnetosphere such that by the end of the simulation run, there is up to a 10 percent fractional change in the Alfvén wave speed and 20 percent change across the noon meridian. While the field line eigenfrequencies are non-stationary, the radial change in eigenfrequency over a grid cell is slightly more than the fractional change due to the increasing Alfvén wave speed, which means the change in the Alfvén wave speed ultimately has no significant impact on our resonance signatures.

2.2. Field Line Resonance Signatures

Figure 3 shows the radial power spectral density of the radial electric field component along the 1500 LT meridian with an overlay of the WKB eigenfrequencies for the odd harmonics, which following Lee et al. [1989] are the only harmonics supported with the driver we have prescribed. The profile extends from just outside the inner boundary at 3 R_E to just beyond the magnetopause–centered around 11 R_E as indicated by the single vertical line–at 11.875 R_E. Figure 4 shows the dynamic cross phase for an identical profile. We calculate the phase of the radial electric field between adjacent radial positions separated by one R_E such that the phase plotted at each radii is the cross phase of the electric field with a radial position one R_E upstream. We use the same two hour time interval to calculate the FFT for each radial position. This is justified because the FLRs are continuously driven and the fractional change in the Alfvén wave speed is inconsequential as discussed above, so the phase changes are appropriately stationary. The alternating bands of 90 to -90 degree phases signify the phase reversals typical of a field line resonance signature for low azimuthal wave number drivers [*Feinrich et al.*, 1997].

2.3. Signatures of Asymmetries in FLR Amplitudes

To observe local time asymmetries in the FLR amplitudes, we calculate the sum of the short-time spectral energies of the radial electric field and compressional magnetic field ratios at [1320,1080], [1440,920], [1500,900], 1520,840], and [1600,800] LTs from the postnoon to prenoon quadrants from one hour long intervals at 10 second sliding increments. We choose a frequency band from 0.5 to 45 mHz and plot the average of every time-window at each radii from 3 to 10.5 R_E every 0.125 R_E as seen in Figure 5. This method calculates the spectral energy across each harmonic spectral resonance width, which is the sum of the overlap of the spatial resonance widths of adjacent resonant L shells. For finite bandwidths the spectral resonance width is simply the Fourier transform of the radial fluid displacements [Mann et al., 1999], so the approach is justified here. We find a persistent bias in the strength of the FLRs in the prenoon quadrant Earthward of L=7 of at least 10 percent with a general increase in the strength of FLRs in the postnoon quadrant moving towards the magnetopause. We also plot in Figure 6 (a) radial electric field ratios as a function of time at the 900 and 1500 LT for the fundamental and third harmonics at L=6 and L=8. Two patterns seem robust in Figure 6: the third harmonic has more energy at L=8 in the postnoon quadrant while the fundamental has more energy at L=6 in the prenoon quadrant, which increases in time. By comparing the radial local time asymmetry between the compressional and radial electric fields, we observe that the compressional field does not seem to be the predominant source controlling the asymmetry in FLR amplitudes.

To estimate the coupling efficiency between the compressional driver to the FLRs, we use a similar procedure outlined above to quantify the local time asymmetry in the electric fields but instead take the ratio of the radial electric field to B_z. Since the difference in fast mode energy across a resonant shell should approximately equal the shear Alfvén energy, we can write $E_{F_0} - E_{F_1} = E_A$, where F_0 is the fast mode energy upstream of the resonant L shell and F_1 is downstream. Noting that the dominate–and readily distinguishable–signatures of the compressional and standing wave modes are B_z and E_r, respectively, ignoring fluid velocities and using Faraday's law we find that $1-\left(\frac{B_{z1}}{B_{z0}}\right)^2 \approx \frac{1}{\omega_r^2(z_0-z_1)^2}\left(\frac{E_r}{B_{z0}}\right)^2$, where ω_r is the resonant frequency at the L shell and $z_0 - z_1$ is the distance along the field line. In ideal MHD the coupling of the wave fields to the fluid displacements should be lossless, thus by evoking the virial theorem, we can justify ignoring the fluid velocities by integrating the fields over time, which should be a good approximation of the wave energy. We plot in Figure 5 (c) the time-averaged estimated coupling efficiency, which we justify averaging after observing a minimal time-variation in coupling efficiency at each radii in Figure 6 (b). We note that the units of this measure of coupling efficiency is in units of velocity, which suggests that the spectral energy in the azimuthal drift balances the resonant coupling of the driver to the standing Alfvén waves. We note a small but persistent local time asymmetry in the coupling efficiency with a bias towards the prenoon quadrant Earthward of L=6 or L=7 and an increase in the efficiency moving from near the noon to the dawk-dusk terminators. This plot, Figure 5 (c), agrees qualitatively with the coupling strengths derived and calculated by Zhu et al. [1988] and Mann et al. [1999].

Dayside equatorial maps of the time-averaged spectral energy of E_r within 5 mHz bands spanning 5-10, 10-15, and 15-20 mHz from the fourth to sixth simulation hours is plotted in Figure 7. These maps include side plots of the radial electric field along meridional and radial rays that cut through the FLR envelopes and highlight the frequency-dependent local time asymmetries in FLR amplitudes shown in Figures 5 and 6.

3. Discussion

3.1. Demonstration of FLRs

Unambiguous evidence of a field line resonance requires a 180 degree phase reversal across an amplitude peak at the resonant L shell. Using stationary point measurements of E_r along the 1500 LT meridian provides convincing evidence in Figures 3 and 4 of a multi-harmonic–1st, 3rd, 5th, continuous FLR spectrum.

Given the linearly increasing fluctuations in the amplitude of the dynamic pressure in the upstream solar wind driver, we must carefully interpret our FLR signatures within the context of the theory developed within the framework of impulsively or steadily-driven FLRs. In particular, the amplitude of the FLRs is an equilibrium at each point in time between the driving energy and ionospheric dampening, which should be appreciable at large L shells here. The saturation widths depend additionally on the phase mixing length, coupling rate, and azimuthal mode number. Feinrich et al. [1997] concluded that the resonance widths for the amplitude and phase change across an FLR should be broad and narrow, respectively [Mann et al., 1995]. However, for drivers with slowly increasing amplitude, the FLR equilibrium amplitude would never approach its asymptotic phase mixing length because the FLR would not decay, and we would expect broad resonance widths, which is consistent with our data. And if the coupling rate were slower than the rate of increase in the amplitude of the fluctuations, the FLR would never reach equilibrium nor saturate. While a quantitative analysis of the actual coupling rate is beyond the scope of this paper, the FLR saturation widths at different time intervals in the simulation are the same, which suggests a constant coupling rate that is faster than the rate of increase in the amplitude of the fluctuations in the driver. The nearly constant coupling efficiency at each radii seen in Figure 6 (b) corrobates this interpretation. Since a qualitative comparison with the radial PSD of E_r from Claudepierre et al. [2010] shows a general agreement even if the mechanisms controlling for their saturation widths are different, this suggests our results with this particular driver are not extraordinary and are consistent with being FLR signatures.

Another issue is whether the grid resolution for this simulation is large enough for SWMF to converge to a physical solution. This is an important consideration because for a given density distribution and ionospheric conductance the asymptotic phase mixing length may conceivably approach the ion gyroradius or smaller, wherein an MHD solution breaks down and a two-fluid or kinetic treatment would become necessary [*Mann et al.*, 1995]. Fortunately, the phase mixing length for the density distribution we have prescribed in this simulation is much larger than a grid cell for the entirety of the magnetospheric cavity. Since the wave amplitude of the driver increases continuously in time, the decay times should be appropriately small, and we can conclude that the phase mixing length is always strictly greater than a grid cell and that the grid resolution is sufficient to resolve FLRs in this simulation.

We observe that the WKB approximation of the field line eigenfrequencies does not accurately align with the first and third harmonics in the radial PSD, but this result is not surprising for a number of reasons. As noted earlier, the eigenfrequencies in this simulation are non-stationary since the Alfvén wave speed linearly decreases through the simulation run time. This is due to an enhancement in the plasma density in the postnoon quadrant with a corresponding density depletion in the prenoon quadrant–a typical signature of a diurnal local time asymmetry [Berube et al., 2003]. Another reason is the WKB approximation is only a first-order solution to the wave equation and does not take into account the more involved wave coupling dynamics that may influence the field line eigenfrequency and saturation widths, such as nonlinear feedback from ponderomotive forces. The WKB approximation, however proves to be a better estimate for the higher order–fifth–harmonics.

3.2. Potential Sources of Asymmetry

The short-time, spatiotemporal spectral energy ratios of the radial electric field show a notable local time, harmonic, and radial asymmetry that's selectively time-dependent. While observational studies have shown before more pronounced meridional asymmetries with a bias in amplitudes towards the prenoon quadrant, its harmonic and radial dependence is an unexpected result here. Here we suggest some plausible mechanisms for particular asymmetries we observe in Figures 5 and 6.

Kelvin-Helmholtz surface waves have loomed larged in studies of dawn-dusk asymmetries in FLR amplitudes. Mann et al. [1999] suggested the generation of Pc5 pulsations driven by KH waves along the dawn magnetopause could generate a prenoon/postnoon asymmetry in FLRs, and Lee and Olson [1980] suggested that the magnetosheath magnetic field, which controls the threshold for the KH instability, can also lead to local time asymmetries. However, since the IMF B_z is due northward and held constant, the latter cannot be a source. The KH generated Pc5 pulsations are a plausible mechanism to explain why the fundamental mode would have more energy in the prenoon quadrant, however the KH waves we observe in our simulation generate Pc5 pulsations that peak at 0.5 mHz, which should not amplify FLRs Earthward of L=10. These pulsations have components in the radial and azimuthal magnetic fields with no additional discernible spectral power in the B_z component. Furthermore, these waves are evanescent and decay rapidly earthward of the magnetopause. For evanescent waves, this cannot explain the sudden reversal in the bias of FLR amplitudes towards the postnoon quadrant sunward of around L=7.

Another explanation we might suggest is that diurnal variations in ionospheric conductance could impact the resonance widths and hence the total amount of energy absorbed per wave period. However, the radial and spectral resonance widths in the prenoon and postnoon quadrants are nearly identical, and this explanation could not explain the harmonic dependence anyway. And as reported by Claudepierre et al. [2010], the radial resonance widths are not responsive to ionospheric conductivity.

Following Southwood [1974], the local density-dependent dampening rate may be responsible for at least some of the observations:

$$\varepsilon = 2\left(\pi\omega\mu_0\Sigma_P \frac{1}{\rho(x_0)}\frac{d\rho(x)}{dx}\right)^{-1}. \tag{2}$$

As seen in Figure 2, the fractional change in number density shows a reduction in density earthward of L=8 in the prenoon quadrant and an increase in density up to L=8 in the postnoon quadrant. Since the amplitude of the radial electric field varies directly with the local mass density [Southwood, 1974], this explains the overall time-dependent bias towards larger FLR amplitudes in the prenoon quadrant earthward of L=8. After inspecting the density sunward of L=7, this cannot be an explanation for the asymmetry profile seen in Figure 5 (b).

Even then, local mass density variations and KH waves along the dawn magnetopause cannot explain why the third harmonic has more power in the postnoon quadrant. In a cold, ideal MHD plasma there should be no dampening or excitation mechanisms except for Joule heating in the ionosphere and leakage of energy downtail, which suggests that the partitioning of energy between wave modes–variations in azimuthal mode number–plays a key role. Wright et al. [1995] used numerical simulations to explore how variations in magnetopause motion impact the phase speed of the driver and its resulting frequency and azimuthal mode spectra. Since for finite wave number the poloidal and toroidal wave modes are coupled, his analysis suggests that meridional asymmetries in the phase speed of magnetopause displacements could generate an azimuthal wave number dependent asymmetry in the frequency spectra, which could explain why the third harmonic would have more energy through the partitioning of more energy into the toroidal mode in the postnoon quadrant. Following this, Lee et al. [1990] offer an explanation for the radially dependent behavior of the FLR amplitudes by suggesting the coupling location, strength and total energy can be mediated by radially-dependent azimuthal mode number spectra due to magnetospheric inhomogeneities. Without an analysis of the local time phase variations along the magnetopause and the mode numbers of each driver we cannot determine if this is the case.

Inspecting Figure 6 (a) shows that amidst the random variations in the time-averaged ratio of the electric fields are statistically significant time-dependent local time asymmetries as well. We observe that the degree of asymmetry in the postnoon to prenoon quadrant over the entire spectral band at L=8 decreases from about 20 percent to near parity after four hours of simulation run time. While the asymmetry in the third harmonic at L=8, for instance, stays relatively constant, there is a persistent increase in the fundamental energy at L=6 in the dawn quadrant from about one percent after the start of the solar wind fluctuations to nearly 15 percent by the end of the simulation. Since the only time-dependent quantities are the increasing amplitude of the compressional driver and the fractional changes in the Alfvén wave speeds, we might suggest that this time-dependent asymmetry grows with the energy of the compressional driver. We cannot explain why this is the case nor why the energy in the third harmonic at L=6 shows no asymmetry until after the fifth hour when suddenly it finds preference towards the postnoon quadrant.

The radially dependent estimated coupling efficiency shows broad agreement with literature. We show additionally that the efficiency exhibits a local time asymmetry and generally increases approaching the dawn-dusk terminator, which has not previously been observed nor predicted. Inspection shows that the local time asymmetry shows a preference for the prenoon quadrant for radii less than 7 R_E, and this follows the radially-dependent asymmetry seen in the electric field ratios. Using the units for field energy shows that the total amount of energy absorbed by the standing Alfvén waves from the compressional driver is less than five percent per resonant point.

4. Conclusion

This study has demonstrated that the SWMF global MHD model can produce and sustain FLRs driven by broadband fluctuations in the dynamic pressure in the upstream solar wind, which validates previous studies such as Claudepierre et al. [2010]. By analyzing the ratio of the radial electric fields across the noon meridian, we also show a radial, harmonic, and time-dependent local time asymmetry in FLR amplitudes. We discussed two paradigms to account for these observations:

1. structural mechanisms such as the azimuthal wave number, phase speed variations along the magnetopause, or local dampening rate due to variations in the equatorial mass density distribution, and

2. additional energy sources such as KH surface waves resonantly coupling to Pc5 band ULF pulsations.

In these cases, we are essentially asking why there is an asymmetry in the compressional driver and time-dependent, meriodional variations in the number density. The ultimate question, however, is whether the 10 to 20 percent difference in FLR power is significant, i.e. not due to random numerical or statistical fluctuations. We would argue that they are because they are persistent–and in some cases time-dependent, dynamic, and relatively large compared against intrinsic asymmetries one might expect in a simulation with a symmetric driver. Distinguishing the impact of these drivers on resonant mode coupling with rigorous statistical methods should be the focus of future studies.

The calculated estimated coupling efficiency we presented is a measure of the amount of spectral energy the compressional driver makes available to the radial electric field. While the total standing Alfvén wave energy includes the azimuthal magnetic field and fluid velocities, this estimate serves as a measure of the time-averaged spectral energy made available to the azimuthal drift of ions. Indeed, it is also a measure of the free wave energy made available for azimuthal acceleration. In terms of energy, at peak efficiency about 10 keV per resonant wave period is made available to ions for azimuthal acceleration. Figure 5 (c) bears remarkable resemblance to L-shell dependent electron intensity profiles used in radiation belt studies, and the peak coupling efficiency between 5 and 6 R_E suggests that an azimuthal electron drift resonance could be ULF wave mediated efficiently via toroidal FLRs in similar global magnetospheric simulations using two-fluid MHD. Even more, the local time asymmetry seen in the coupling efficiency predicts and offers an explanation for any azimuthal asymmetries in radiation belt intensities. This may be explored in future studies.

Lastly, the local time and radial asymmetry seen in the fractional changes in the number density appears to be related to natural diurnal variations in equatorial mass density. However, given the remarks above concerning the coupling efficiency and the fluctuations and radially-dependent monotonic behavior seen in Figure 2 entertain whether this is driven by ULF wave dynamics and the amplitude asymmetries. While it is possible that the waves generated in this simulation could mediate the equatorial mass density distribution through radial diffusion, amplification of the convective electric field and azimuthal drifts, we have already concluded that the local dampening rates are density dependent and would affect the FLR amplitude asymmetries as well. How these forces interact to shape the equilibrium FLR amplitudes and mass density distribution is an unresolved question.

Acknowledgments. The data for this paper are made available upon request from SME (sidneye@umich.edu). SME would like to thank his thesis adviser Mark Moldwin for his steadfast support and excellent mentoring and postdoc Michael Hartinger for his enlightening discourse. NASA grants NNX11Ao60G and NNX10AQ53G partially supported this research.

5. References

Bellan, P.M. (1996), Mode conversion into non-MHD waves at the Alfven layer: The case against the field line resonance concept, *Journal of Geophysical Research: Space Physics*, 101(A11).

Berube, D., Moldwin, M.B., and Weygand J.M. (2003), An automated method for the detection of field line resonance frequencies using ground magnetometer techniques, *Journal of Geophysical Research: Space Physics*, 108(A9), 1348, doi:10.1029/2002JA009737.

Cheng, C.Z., and Q. Qian (1994), Theory of ballooning-mirror instabilities for anisotropic pressure plasmas in the magnetosphere, *Journal of Geophysical Research: Space Physics*, 99(A6), 11193-11209, doi: 10.1029/94JA00657.

Chi, P.J., and C.T. Russell (1998), Phase skipping and Poynting flux of continuous pulsations, *Journal of Geophysical Research: Space Physics*, 103(A12), 29479-29491, doi: 10.1029/98JA02101.

Chisham, G., and Orr, D. (1997), A statistical study of the local time asymmetry of Pc5 ULF wave characteristics observed at midlatitudes by SAMNET, *Journal of Geophysical Research: Space Physics*, 102(A11), 24339-24350, doi: 10.1029/97JA01801.

Claudepierre, S.G., M.K. Hudson, W. Lotko, J.G. Lyon and R.E. Denton (2010), Solar wind driving of magnetospheric ULF waves: Field line resonances driven by dynamic pressure fluctuations, *Journal of Geophysical Research: Space Physics*, 115(A11), doi: 10.1029/2010JA015399.

Degeling, A.W., R. Rankin, K. Kabin, I.J. Rae and F.R. Fenrich (2010), Modeling ULF waves in a compressed dipole magnetic field, *Journal of Geophysical Research: Space Physics*, 115(A10), doi: 10.1029/2010JA015410.

Elkington, S. R., M. K. Hudson, and A. A. Chan (1999), Acceleration of relativistic electrons via drift-resonant interaction with toroidal-mode Pc-5 ULF oscillations, *Geophysical Research Letters*, 26, 3273.

Engebretson, M.J., L.J. Zanetti, T.A. Potemra, W. Baumjohann, H. Lhr and M.H. Acuna (1987), Simultaneous observation of Pc 3-4 pulsations in the solar wind and in the Earth's magnetosphere, *Journal of Geophysical Research: Space Physics*, 92(A9), 10053-10062, doi: 10.1029/JA092iA09p10053.

Feinrich, F.R., and J.C. Samson (1997), Growth and decay of field line resonances, *Journal of Geophysical Research: Space Physics*, 102(A9), 20031-20039, doi:10.1029/97JA01376.

Glassmeier, K.H. and Stellmacher, M. (2000), Concerning the local time asymmetry of Pc5 wave power at the ground and field line resonance widths, *Journal of Geophysical Research: Space Physics*, 105(A8), 18847-18855, doi: 10.1029/2000JA900037.

Hasegawa, Akira (1969), Drift Mirror Instability in the Magnetosphere, *Physics of Fluids* (1958-1988), 12, 2642-2650, doi:http://dx.doi.org/10.1063/1.1692407

Kivelson, M.G., and D.J. Southwood (1986), Coupling of global magnetospheric MHD eigenmodes to field line resonances, *Journal of Geophysical Research: Space Physics*, 91(A4), 4345-4351, doi: 10.1029/JA091iA04p04345.

Lee, D., and R.L. Lysak (1990), Effects of azimuthal asymmetry on ULF waves in the dipole magnetosphere,*Geophysical Research Letters*, 17(1), 53-56, doi: 10.1029/GL017i001p00053.

Lee, L. C., and J. V. Olson (1980), Kelvin-Helmholtz Instability and the Variation of Geomagnetic Pulsation Activity, Geophysical Research Letters, 7(10), 777-780.

Mann, I.R., A.N. Wright and P.S. Cally (1995), Coupling of magnetospheric cavity modes to field line resonances: A study of resonance widths, *Journal of Geophysical Research: Space Physics*, 100(A10), 19441-19456, doi: 10.1029/95JA00820.

Mann, I.R., and A.N. Wright (1999), Diagnosing the excitation mechanisms of Pc5 magnetospheric flank waveguide modes and FLRs, *Geophysical Research Letters*, 26, 16, 2609-2612, doi: 10.1029/1999GL900573.

Mann, I.R., A.N. Wright, K.J. Mills and V.M. Nakariakov (1999), Excitation of magnetospheric waveguide modes by magnetosheath flows, *Journal of Geophysical Research: Space Physics*, 104(A1), 333-353, doi: 10.1029/1998JA900026.

Newton, R.S., D.J. Southwood and W.J. Hughes (1978), Damping of geomagnetic pulsations by the ionosphere, *Planetary Space Sciences*, 26(3), 201-209, doi:10.1016/0032-0633(78)90085-5.

Nosé, M., Iyemore, T., Sugiura, M., and Slavin, J.A. (1995), A strong dawn/dusk asymmetry in Pc5 pulsation occurrence observed by the DE-1 satellite, *Geophysical Review Letters*, 22, 15 2053-2056, doi: 10.1029/95GL01794.

Radoski, H.R., and R.L. Carovillano (1966), Axisymmetric Plasmasphere Resonances: Toroidal Mode, *Physics of Fluids*, 9(2), 285, doi: 10.1063/1.1761671.

Samson, J.C., B.G. Harrold, J.M. Ruohoniemi, R.A. Greenwald and A.D.M. Walker (1992), Field line reasonance associated with MHD waveguides in the magnetosphere, *Geophysics Research Letters*, 19, 441.

Sarris, T.E., T. E. Sarris, A. N. Wright and X. Li (2009), Observations and analysis of Alfvén wave phase mixing in the Earth's magnetosphere, *Journal of Geophysical Research*, 114(a3), A03218.

Southwood, D.J. (1974), Some features of field line resonances in the magnetosphere, *Planetary Space Sciences*, 22, 483-491.

Southwood, D.J., and M.G. Kivelson (1990), The magnetohydrodynamic response of the magnetospheric cavity to changes in solar wind pressure, *Journal of Geophysical Research: Space Physics*,95(a3), 2301-2309.

Stellmacher, M., K., Glassmeier, R.L. Lysak and M.G. Kivelson (1997), Field line resonances in discretized magnetospheric models: an artifact study, *Annals Geophysicae*, 15(6), 614-624, doi: 10.1007/s00585-997-0614-0.

Takahashi, K., T. A. Potemra, R. W. McEntire, L. J. Zanetti, and L. M. Kistler (1988), Magnetospheric ULF waves observed during the major magnetospheric compression of November 1, 1984, *Journal of Geophysical Research: Space Physics*, 93, 14,36914,382, doi:10.1029/JA093iA12p14369.

Toth, G., I.V. Sokolov, T.I. Gombosi, D.R. Chesney, C.R. Clauer, D.L. De Zeeuw, K.C. Hansen, K.J. Kane, W.B. Manchester, R.C. Oehmke, K.G. Powell, A.J. Ridley, I.I. Roussev, Q.F. Stout, O. Volberg, R.A. Wolf, S. Sazykin, A. Chan, B. Yu and J. Kta (2005), Space Weather Modeling Framework: A new tool for the space science community, *tJournal of Geophysical Research: Space Physics*, 110(A12), - A12226, doi: 10.1029/2005JA011126.

Wright, A.N. and Rickard G.J. (1995), ULF pulsations driven by magnetopause motions: azimuthal phase characteristics, *Journal of Geophysical Research: Space Physics*, 100(A12), 23703-23710, doi: 10.1029/95JA011765.

Zhu, X. and Kivelson, M.G. (1988), Analytic formulation and quantitative solutions of the coupled ULF wave problem, *Journal of Geophysical Research: Space Physics*, 93(A8), 8602-8612, doi: 0.1029/JA093iA08p08602.

Figure 1: Synthetic upstream solar wind dynamic pressure with power spectral density in inset.

Figure 2: Fractional change in the number density at various radii along the 900 and 1500 LT meridians.

Figure 3: Radial PSD profile of the radial electric field with WKB estimates of the field line eigenfrequency harmonics overlaid. Magnetopause location is indicated by the single, black vertical line.

Figure 4: Radial cross-phase profile of radial electric field with WKB estimates of the field line eigenfrequency harmonics overlaid. Magnetopause location is indicated by the single, black vertical line.

Figure 5: (a) and (b) Local time asymmetry as a function of radii for the compressional magnetic field and radial electric field ratios and (c) estimated measures of the coupling efficiency along meridians spanning from 800 to 1600 LT.

Figure 6: (a) The local time asymmetry as a function of time for the radial electric field ratios between the 1500 and 900 LT meridians; (b) the estimated measure of coupling efficiency at various radii and harmonic bands at the 900 and 1500 LT meridians.

Figure 7: Contour plot is an equatorial map of the spectral energy of the radial electric field in 5 mHz bands. The fields are time-averaged over a 2.5 hour interval from roughly the fourth to sixth hour of simulation time. The bottom side plots show the sampled radial electric fields at 0.125 Earth radii increments along the 1000 LT and 1400 LT meridians. The left side plots show the sampled radial electric fields at 1 degree increments at the color-coded radii from 600 to 1800 LT.

Table 1. Comparison of Input Parameters

Inputs	**LFM**	**SWMF**
Grid, Resolution	Distorted Spherical, 0.25 R_E	Cartesian, 0.125 R_E
Solar wind Velocity	-600 km/s	-400 km/s
Inner Boundary	2.2 R_E	2.5 R_E
Pedersen Conductance	5 S	0.25 S

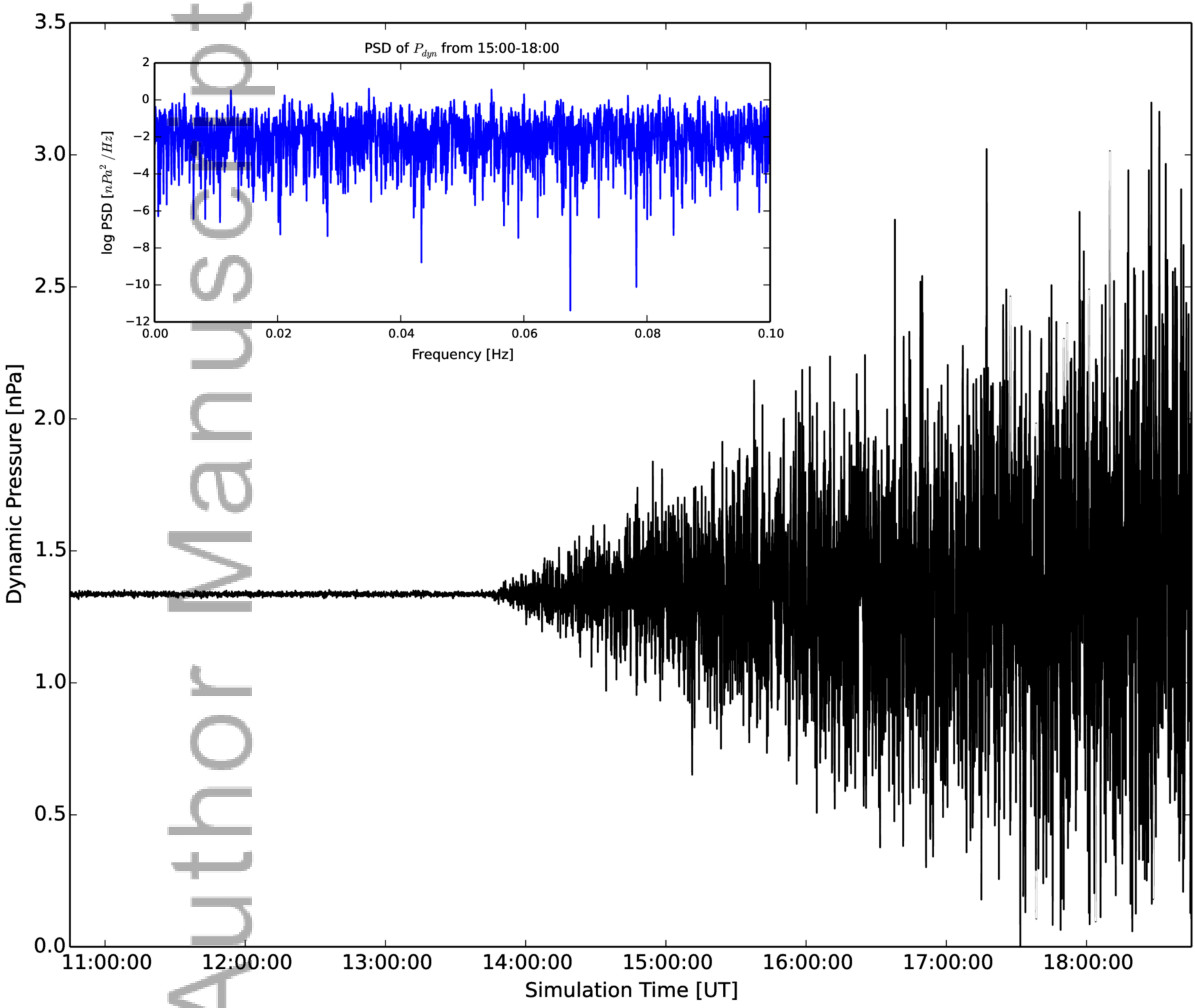

2015ja021920-f00-z-

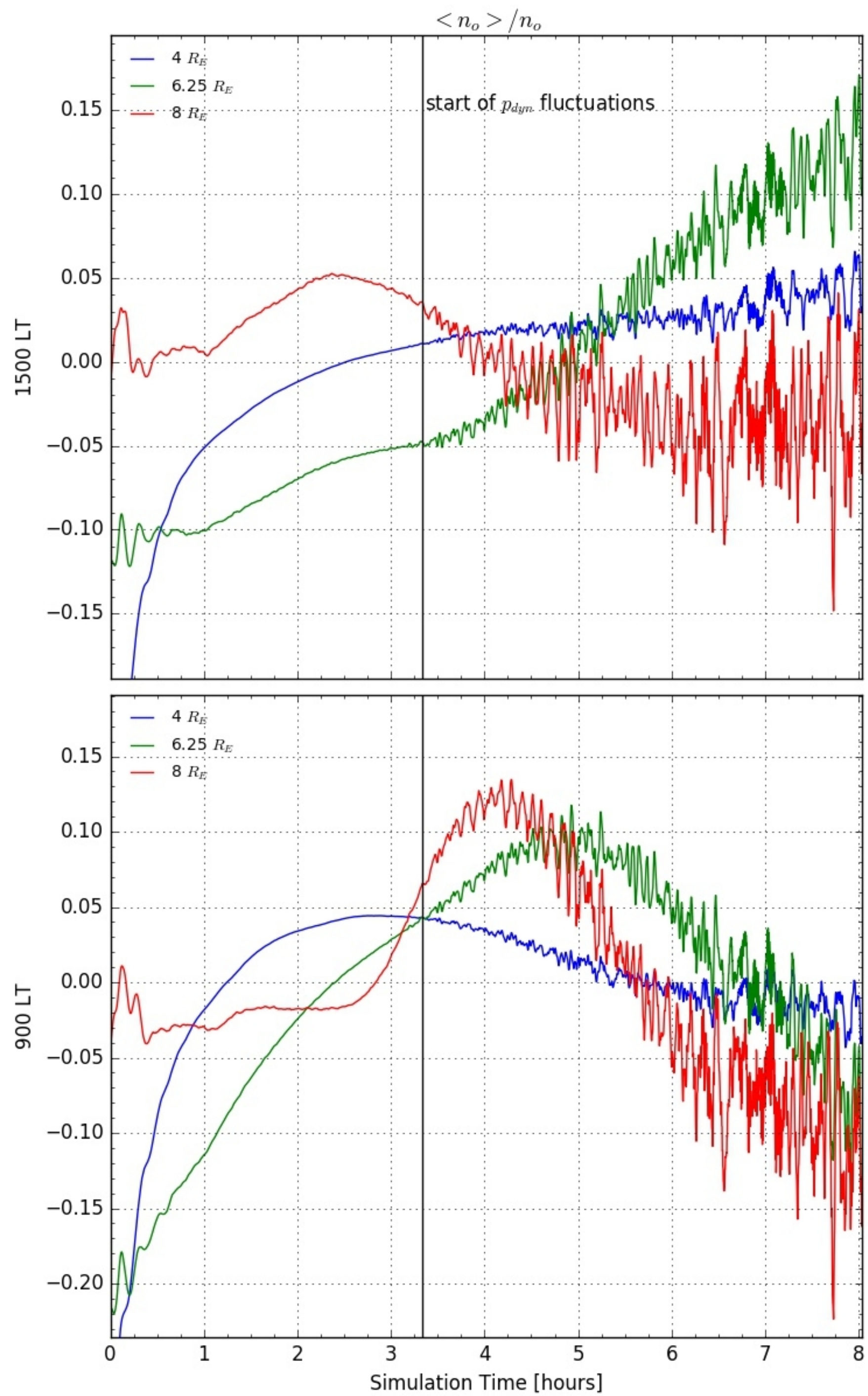

$< n_o > / n_o$
4 R_E
6.25 R_E
8 R_E
start of p_{dyn} fluctuations
1500 LT
0.15
0.10
0.05
0.00
−0.05
−0.10
−0.15
4 R_E
6.25 R_E
8 R_E
900 LT
0.15
0.10
0.05
0.00
−0.05
−0.10
−0.15
−0.20
0
1
2
3
4
5
6
7
8
Simulation Time [hours]

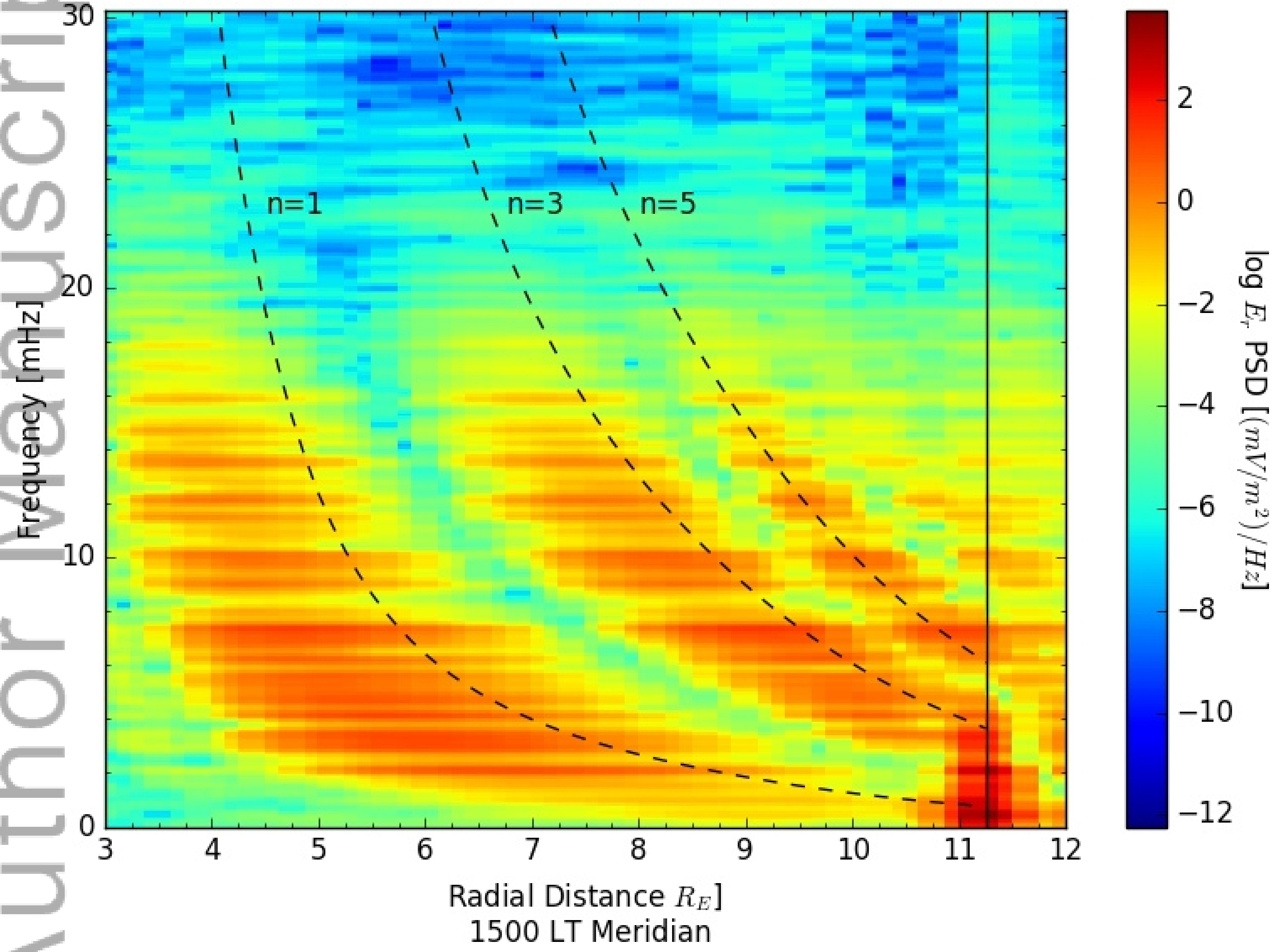
30
20
10
0
Frequency [mHz]
3
4
5
6
7
8
9
10
11
12
Radial Distance R_E]
1500 LT Meridian
n=1
n=3
n=5
2
0
−2
−4
−6
−8
−10
−12
log E_r PSD [$(mV/m^2)/Hz$]

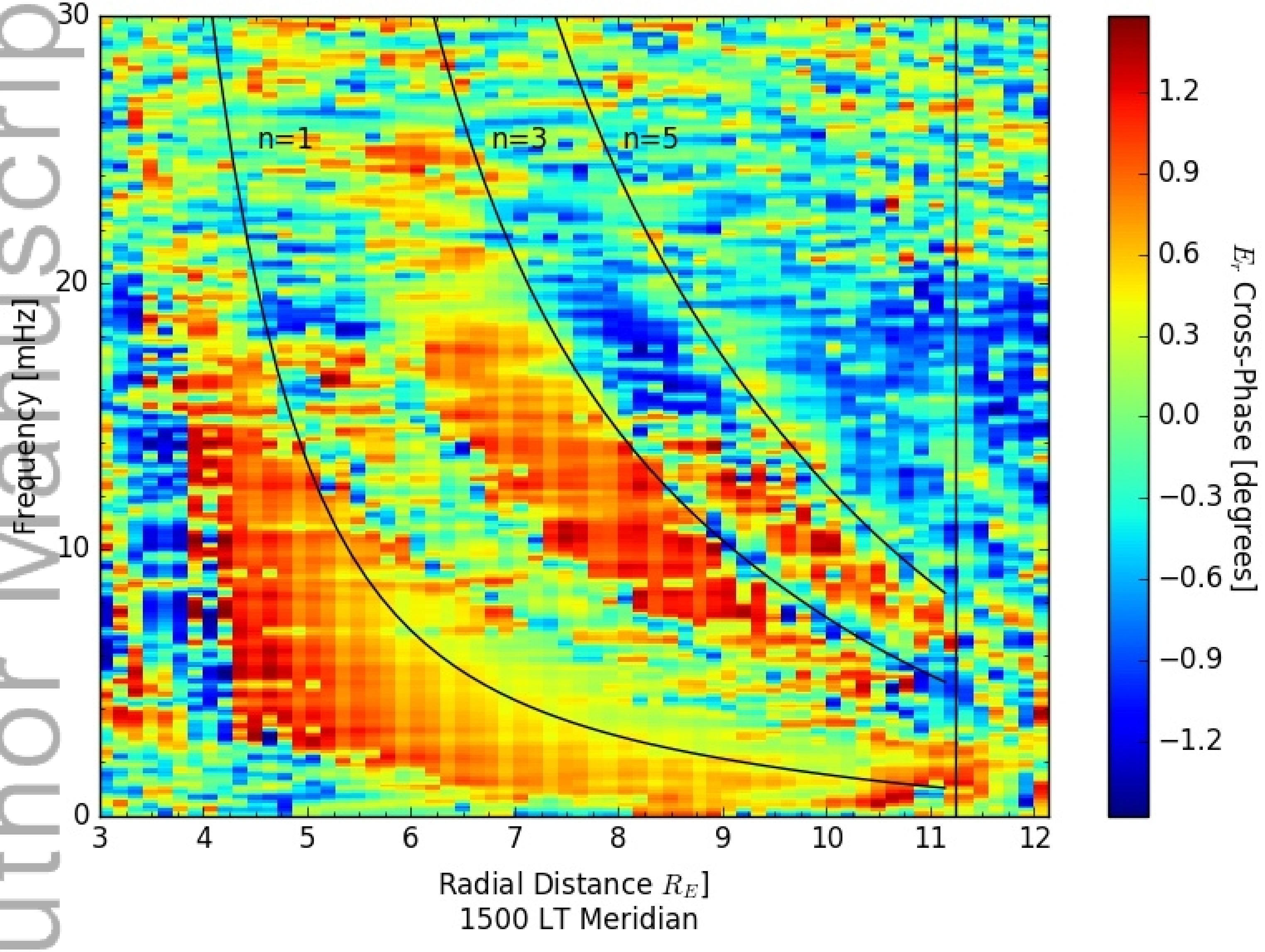

30
20
10
0
Frequency [mHz]
3
4
5
6
7
8
9
10
11
12
Radial Distance R_E]
1500 LT Meridian
n=1
n=3
n=5
1.2
0.9
0.6
0.3
0.0
−0.3
−0.6
−0.9
−1.2
E_r Cross-Phase [degrees]

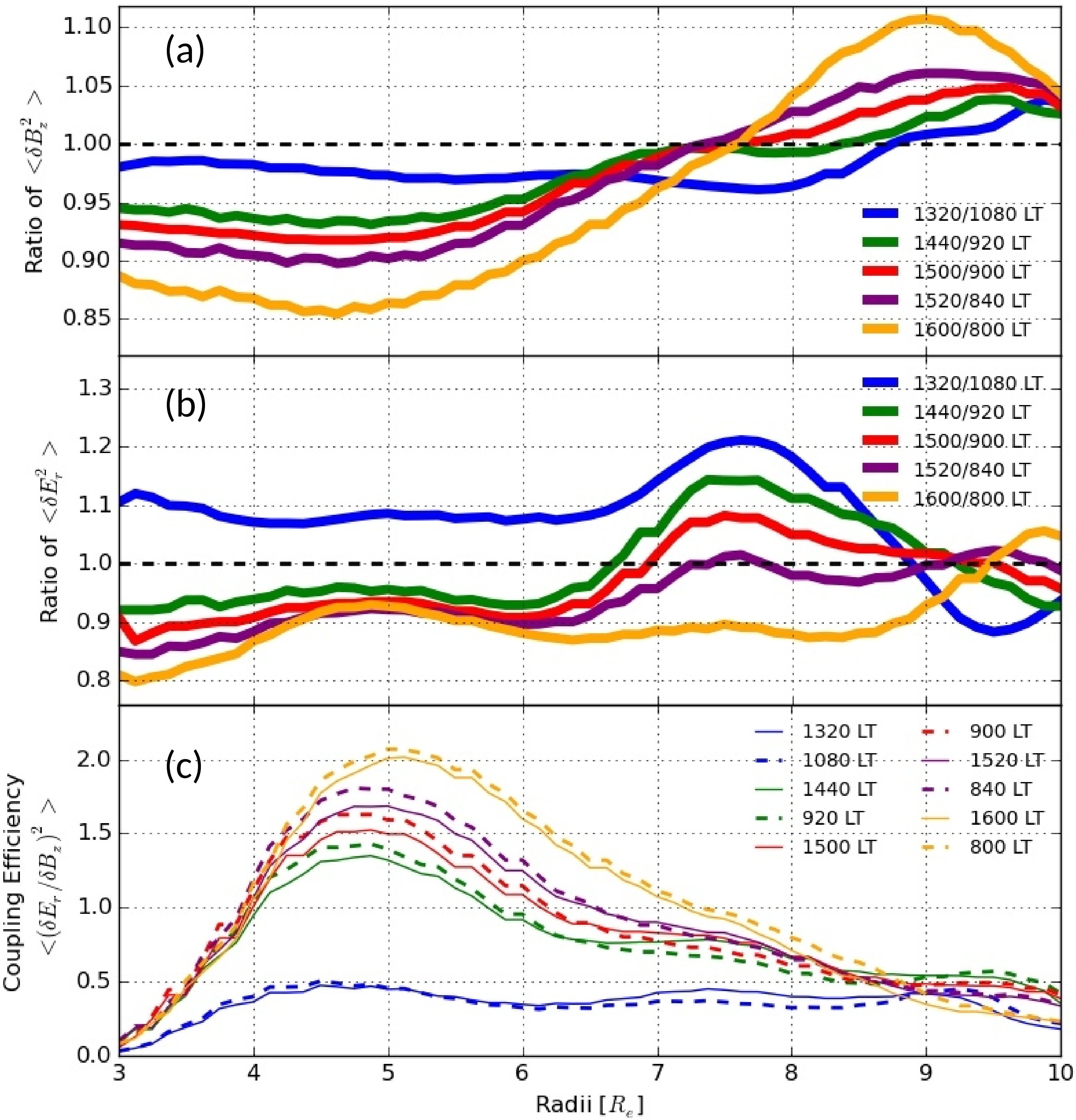
(a)
Ratio of $<\delta B_z^2>$
1.10
1.05
1.00
0.95
0.90
0.85
1320/1080 LT
1440/920 LT
1500/900 LT
1520/840 LT
1600/800 LT
(b)
Ratio of $<\delta E_r^2>$
1.3
1.2
1.1
1.0
0.9
0.8
1320/1080 LT
1440/920 LT
1500/900 LT
1520/840 LT
1600/800 LT
(c)
Coupling Efficiency $<(\delta E_r/\delta B_z)^2>$
2.0
1.5
1.0
0.5
0.0
1320 LT
1080 LT
1440 LT
920 LT
1500 LT
900 LT
1520 LT
840 LT
1600 LT
800 LT
3
4
5
6
7
8
9
10
Radii $[R_e]$

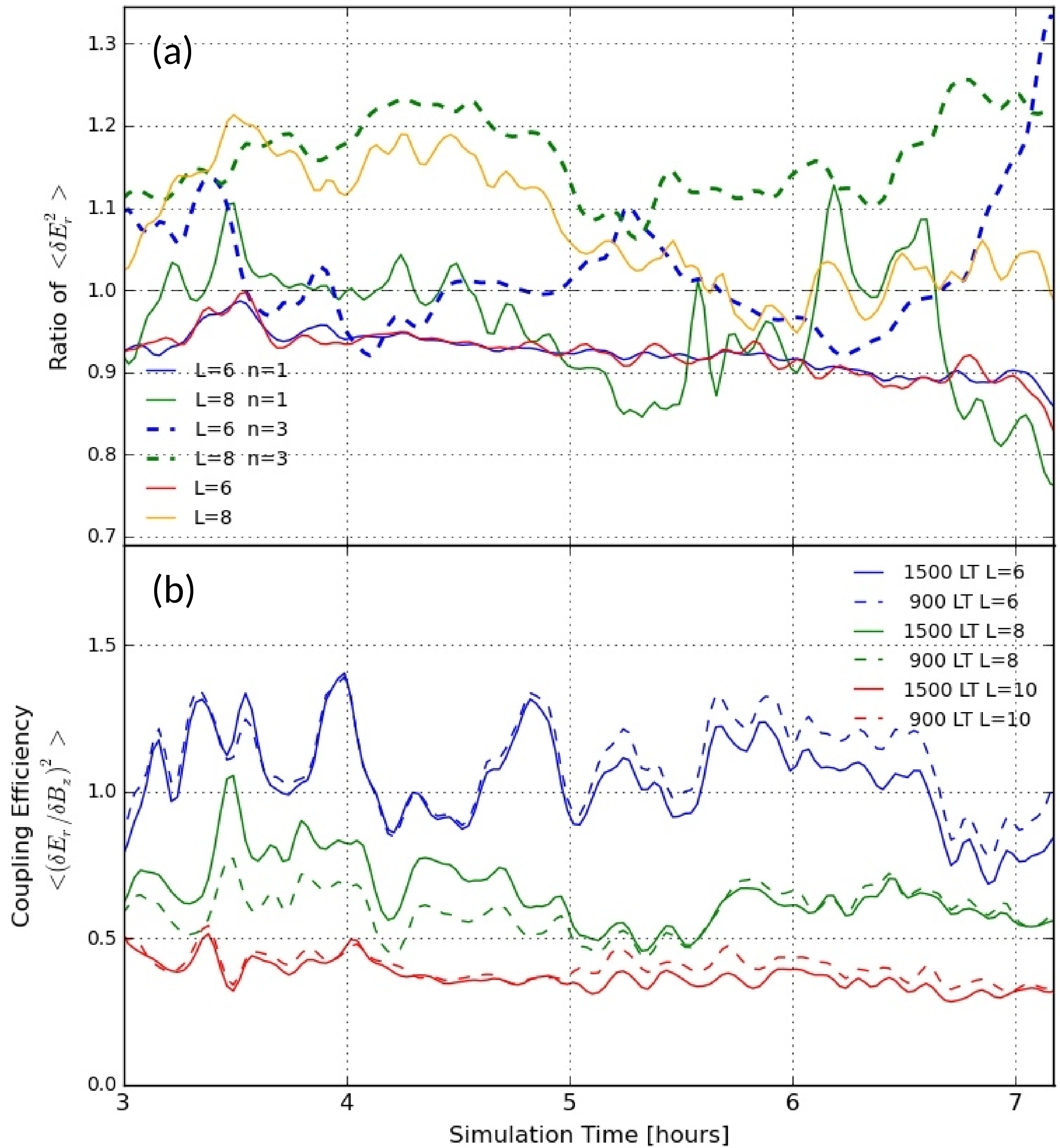
(a)
Ratio of $<\delta E_r^2>$
L=6 n=1
L=8 n=1
L=6 n=3
L=8 n=3
L=6
L=8
(b)
Coupling Efficiency $<(\delta E_r/\delta B_z)^2>$
1500 LT L=6
900 LT L=6
1500 LT L=8
900 LT L=8
1500 LT L=10
900 LT L=10
Simulation Time [hours]

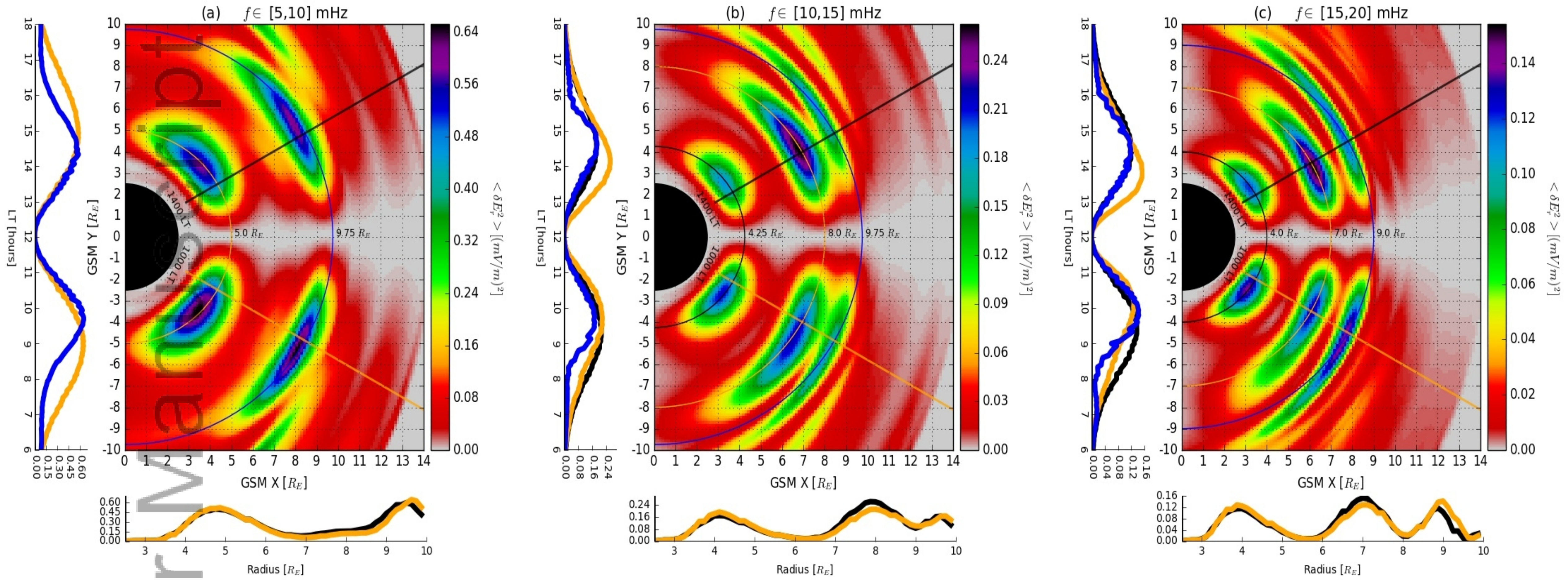

(a) $f \in$ [5,10] mHz
(b) $f \in$ [10,15] mHz
(c) $f \in$ [15,20] mHz
GSM Y [R_E]
GSM X [R_E]
LT [hours]
Radius [R_E]
$<\delta E_r^2> [(mV/m)^2]$
1400 LT
1000 LT
5.0 R_E
9.75 R_E
4.25 R_E
8.0 R_E
4.0 R_E
7.0 R_E
9.0 R_E